Three-Dimensional Numerical Modeling of the Temporal Evolution of Backward Erosion Piping

Zhijie Wang^{a,*}, Caglar Oskay^b, Alessandro Fascetti^a

^aDepartment of Civil and Environmental Engineering, University of Pittsburgh,
 742 Benedum Hall, Pittsburgh, 15261, Pennsylvania, USA
 ^bDepartment of Civil and Environmental Engineering, Vanderbilt University,
 2301 Vanderbilt Place, Nashville, 37235-1831, Tennessee, USA

Abstract

Backward erosion piping (BEP) is a complex degradation mechanism in geotechnical flood protection infrastructure (GFPI) that is still relatively less understood, particularly when considering its time-dependent features. This manuscript presents a novel dual random lattice modeling (DRLM) approach for three-dimensional simulation of BEP, with a focus on its evolution over time. The key novelty of this presented framework is twofold: (1) we propose and incorporate a novel constitutive relationship for computation of time-dependent soil erosion based on the theory of rate processes, and (2) we devise an algorithm for calculation of coupled degradation of the dual lattices for accurate computation of 3-D hydraulic gradients. The constitutive relationship was developed from fundamental granular physics, and brings the potential to provide deeper fundamental physical understanding of the phenomenon. The capabilities of the modeling framework are investigated

^{*}Corresponding author.

Email addresses: zhijiewang@pitt.edu (Zhijie Wang), caglar.oskay@vanderbilt.edu (Caglar Oskay), fascetti@pitt.edu (Alessandro Fascetti)

by comparison with available laboratory experiments which illustrates good agreement in the spatial advancement of piping erosion, pipe progression speeds, as well as the evolution of local gradients. To the best knowledge of the authors, the presented model is the first to be able to capture all of the aforementioned features when simulating BEP.

Keywords: backward erosion piping, numerical modeling, constitutive law, time evolution, computational algorithm

1. Introduction

Flooding has been identified as the most common and costly source of natural risk in the United States and worldwide (FEMA, 2019). Piping is reported to be responsible for nearly half of all documented geotechnical flood protection infrastructure (GFPI) failures and among different types of piping incidents nearly one third are attributed to backward erosion piping (BEP) (Foster et al., 2000; Richards and Reddy, 2007). BEP refers to continuous removal of particles by seepage flow in saturated sandy soils, so that an open pipe initiates and progresses from the downstream side upwards (Richards and Reddy, 2007, 2012). BEP is usually initiated by flow exit conditions on the downstream side of the system, where flow concentrations occur and lead to sand boils (Fleshman and Rice, 2013; van Beek et al., 2015).

Although several research groups have studied BEP from an analytical and experimental point of view, the fundamental mechanisms of pipe initiation and progression, and characterization of their spatial and temporal features still pose significant challenges in the design and operation of GFPI.

This is due to the fact that BEP is a complex physical process which involves the interactions of soil mechanics, fluid mechanics and sediment transport (Schmertmann, 2000). Focus of some of these studies has been on developing models for identification of factors of safety for GFPIs against BEP. Aided by experimental observations, previous authors developed empirical or semi-analytical models for identifying a threshold hydraulic gradient, shear stress, or flow velocity which represents the critical hydraulic conditions in the structures (Bligh, 1910; Fleshman and Rice, 2013; Negrinelli, 2015; Ojha et al., 2003; Peng and Rice, 2020; Reddi et al., 2000; Schmertmann, 2000; Sellmeijer, 1988; van Beek, 2015; van Beek et al., 2010). In order to characterize temporal evolution of BEP, a number of experimental investigations studied pipe progression rates at small and medium scales (Allan, 2018; Pol et al., 2021; Robbins et al., 2018; Vandenboer et al., 2019). Formal methodologies to apply these findings to field conditions have not been achieved due to the effects of soil variability and complexity in hydraulic conditions in the field (Negrinelli et al., 2016). Numerical modeling serves as a complementary tool to study BEP, particularly for detailed characterization of its spatial and temporal evolution.

Several numerical models have been previously proposed to deepen understanding of the physical mechanisms governing BEP. As summarized by Wang et al. (2014), the BEP numerical models in the literature can be grouped into three categories based on their representations of the erosion process: (1) homogenized continuum formulations based on seepage analysis, with or without schemes to update hydraulic conductivity as a result of erosion (Hagerty and Curini, 2004; Rahimi et al., 2021), (2) models formu-

lated with discrete element method (DEM) (Zeghal and El Shamy, 2004; El Shamy and Aydin, 2008), and (3) multi-phase models describing the interaction between the fluid phase and solid skeleton (Bonelli and Benahmed, 2010; Fascetti and Oskay, 2019b; Fujisawa et al., 2010). Despite progress made by these contributions, the following three aspects remain to be outstanding challenges: (1) capturing the three dimensional characteristics of the phenomenon (Robbins and Griffiths, 2021), as the majority of available studies have primarily focused on two-dimensional configurations, (2) describing random features of BEP propagation (Rotunno et al., 2019; van Beek, 2022), as several existing models constrain the erosion paths based on mesh contours or define the path a priori, and (3) deriving a physics-based description of the relationship between erosion rate and local hydraulic conditions, since available models largely employ semi-analytical descriptions of BEP derived from limited experimental observations.

Earlier empirical studies and recent semi-analytical investigations adopted different forms of linear relationships between the shear stress exerted onto the erodible particles by the seepage flow and the erosion rate in the soil (Khilar et al., 1985; Reddi et al., 2000; Indraratna et al., 2009). These studies hinge on the fundamental assumption that BEP is controlled by the particle erosion at the walls of the established pipe under seepage flow (the so-called secondary erosion, according to Hanses (1985)). However, Allan (2018) pointed out that pipe progression is more likely to be dominated by soil erosion at the pipe tip (primary erosion, according to Hanses (1985)) instead. Moreover, in the vicinity of the pipe tip, no consensus has been reached as to which directional component of the seepage flow, vertical or

horizontal, controls mobilization of particles (i.e., erosion rate) (Allan, 2018).

This makes formulations of constitutive relations for the erosion rate a challenging task when devising strategies based on hydraulic loading measures such as hydraulic gradient or shear stress. In recent investigations, Sibille et al. (2015) and Kodieh et al. (2021) devised a novel energy-based framework for predicting erosion rates, as measured in internal erosion tests, from fundamental principles based on fluid mechanics. This provides an alternative approach for erosion rate estimation at the pipe tip where complex 3D equilibrium conditions exist.

Available computational approaches capable of describing temporal development of piping in the simulations include the transient groundwater flow model (van Esch et al., 2013), erosion rates-based model for hole erosion test simulation (Bonelli and Benahmed, 2010), a bed-load transport model in laminar flow (Cheng, 2004), and models focusing on pipe progression speed (Fujisawa et al., 2010; Rotunno et al., 2019; Wang et al., 2014). However, in all these works, the erosion rates are generally estimated from the aforementioned semi-analytical shear stress-/gradient-based approaches (Bonelli and Benahmed, 2010; Cheng, 2004; Fujisawa et al., 2010; Rotunno et al., 2019; Wang et al., 2014). Moreover, there still exists a fundamental lack of validation against experimental results, particularly for what concerns the time-dependent characteristics of BEP (Cheng, 2004; van Esch et al., 2013).

The primary contribution of this manuscript is a new dual random lattice formulation that is capable of modeling time evolution of backward erosion

The primary contribution of this manuscript is a new dual random lattice formulation that is capable of modeling time evolution of backward erosion piping (BEP) in three dimensions. The central motivation and novelty of this work are discussed prior to the systematic presentation of the govern-

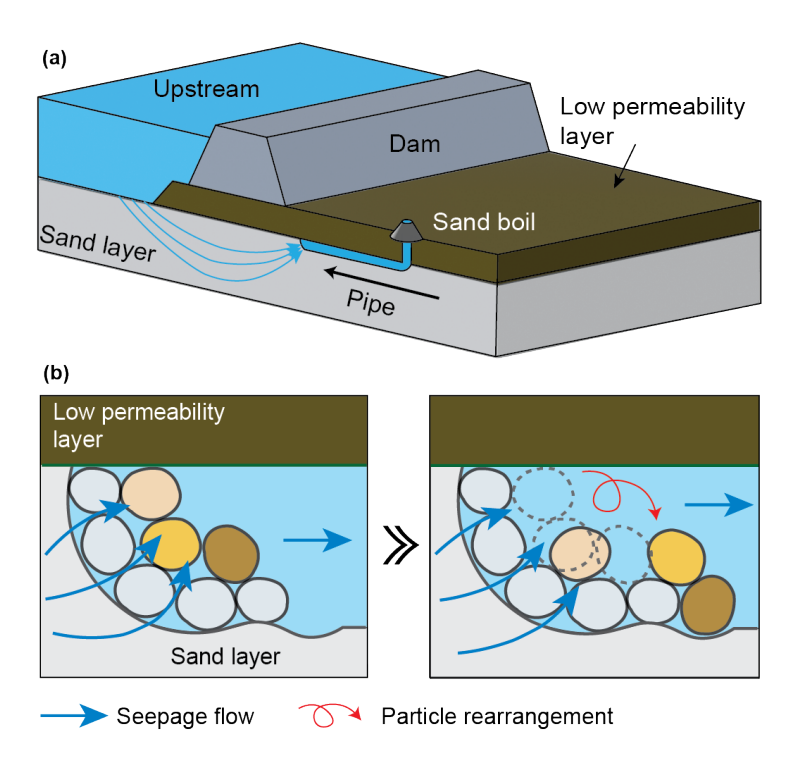


Figure 1: Schematic of BEP initiation and progression: (a) overview, and (b) soil erosion at pipe tip via successive particle rearrangement

ing equations, which encompass those for describing hydraulic dynamics as a transport problem and estimating soil erosion rates based on the theory of rate processes. The following section introduces the implementation of simulations with the model and proposes an algorithm for accurately calculating interdependent changes in permeability properties due to soil erosion across dual lattice networks. Lastly, the manuscript presents and discusses comparisons of simulation results with one set of available experimental findings, serving to evaluate the proposed model's capacity to accurately simulate BEP.

2. Motivation and Novelty

104

107

109

111

114

115

116

121

123

124

Although time evolution of BEP is critical for GFPI safety, relatively less 103 attention has been given to it in comparison with identifying critical hydraulic loading conditions associated with BEP initiation. Capability of describing 105 the pipe progression speed would enable prediction of the time required for 106 a pipe to reach upstream side, as well as unveil fundamental mechanisms governing the phenomenon. This capability would enable evaluation of the risk for full pipe development for a given flood duration or estimation of how many flood events a given dam/levee could survive if past flood levels and duration are available in flood hydro-graphs (Allan, 2018).

To this end, this study develops a three-dimensional numerical method 112 capable of accurately simulating time evolution of BEP in GFPI. Figure 1 illustrates the BEP process at system scale (Fig. 1(a)) and time-dependent particle erosion at micro-scale. As shown in Fig. 1(b), we hypothesize that BEP progression is driven by particle erosion at the pipe tip as a result of successive particle rearrangements under seepage flow, such that erosion can be described as a rate process. A new constitutive relationship, based on the theory of rate processes, is then adopted to estimate erosion rate in the soil as a function of the seepage flow energy. This constitutive relationship is incorporated into a dual random lattice model (DRLM). The proposed numerical method is then evaluated by means of comparison with available highly instrumented laboratory tests.

The key novel contributions of this work are: (1) the development of a constitutive relationship for computation of soil erosion rate under seepage based on fundamental granular physics and incorporating this relationship into a 3-dimensional DRLM approach, and (2) the definition of a new methodology for calculation of coupled degradation on dual lattice networks.

29 3. Governing Equations

137

3.1. Nonlinear Transport Problem

Erosion in porous media (i.e., aquifers) can be described as a transport problem using a non-linear diffusion equation (Fascetti and Oskay, 2019a; Hagerty and Curini, 2004; Robbins, 2016; Vandenboer et al., 2014):

$$\frac{\partial h(\mathbf{x},t)}{\partial t} = \nabla \cdot (D(h(\mathbf{x},t))\nabla h(\mathbf{x},t)) \qquad \mathbf{x} \in \mathbf{\Omega}, t \in (0,T)$$
 (1)

where h represents the hydraulic head field, Ω the computational domain, T the total time, and $D = k/S_S$ the soil diffusivity coefficient, which is related the hydraulic conductivity and specific storage (Green and Wang, 1990).

The domain is subjected to the following prescribed boundary conditions:

$$h = h_B(t) \qquad \text{on } \Gamma_b \subset \partial \Omega$$

$$\mathbf{q} \equiv -D \frac{\partial h}{\partial \mathbf{n}} = \mathbf{q}_B \qquad \text{on } \Gamma_q \subset \partial \Omega$$
(2)

with $\Gamma_b \cap \Gamma_q = \emptyset$, \mathbf{q}_B is the prescribed outward flux orthogonal to the domain boundary with normal \mathbf{n} , and h_B the time-dependent prescribed hydraulic head at the boundary. Under assumption of laminar flow, Darcy's law and the Kozeny-Carman equation can be utilized to complement the previous equation and estimate hydraulic conductivity of the soil from its porosity (White, 1940; van Beek, 2015). It is worth mentioning that the assumptions of laminar flow and the applicability of Darcy's law in the context of backward erosion piping have been validated through both experimental and numerical studies on sandy soils, as reported in Sellmeijer (1988), van Beek et al.
(2015), and Robbins and Griffiths (2021). While the behavior of seepage flow
at microscopic scale may deviate from laminar flow, at the scale of the control volume employed in the numerical simulations, these assumptions have
been demonstrated to be valid.

3.2. Soil Erosion As A Rate Process

The theory of rate processes was originally developed for describing ki-152 netics of chemical reactions and was systematically summarized in Eyring (1936) and Glasstone et al. (1941). The theory later found successful applica-154 tions in describing rates of different processes in soils involving rearrangement of granular matter, such as creep, shear deformation, and surface soil erosion (Gularte et al., 1980; Mitchell, 1964; Mitchell et al., 1968; Michalowski 157 et al., 2018). The observations of BEP in various experimental studies ex-158 hibit traits that are usually observed in rate processes, such as stochasticity, 159 "step-wise" pipe progression, and non-linear acceleration of pipe advancement over time (Robbins et al., 2018; van Beek et al., 2015). In view of these 161 traits, Wang et al. (2024) proposed a constitutive relationship between the 162 energy density of seepage flow and the soil erosion rate in the aquifer dur-163 ing BEP based on the theory of rate processes. As postulated in this work, mobilization of the particles involves sliding and/or rolling at inter-particle 165 contacts, which involves crossings of energy barriers formed by confinements 166 exerted by neighboring particles (see Fig. 1(b)). 167

Previous studies employed the hydraulic shear stress to estimate the erosion rate by assuming that detachment of particles occurs primarily on walls

of the pipe, rather than in the vicinity of the pipe tip (Bonelli and Benahmed, 2010; Cheng, 2004; Fujisawa et al., 2010; Rotunno et al., 2019). However, as 171 pointed out by Allan (2018), soil erosion is more likely a result of particle mobilizations at the pipe tip where seepage flows exhibits complex three-173 dimensional traits, which not only reduce applicability of shear stress-based 174 relationships, but also impose challenges in resolving the local hydraulic con-175 ditions. Based on this reasoning, energetic principles are adopted in this 176 study as the fundamental metric for devising a three-dimensional constitutive relationship that describes the erosion rate as a function of the energy expended by the flow. The flow power, P_{flow} , in a control volume is given 179 by (Gelet and Marot, 2022; Kodieh et al., 2021; Marot et al., 2012; Sibille et 180 al., 2015): 181

$$P_{flow} = -\int_{S_i} (p \mathbf{v} \cdot \mathbf{n}_i + \gamma_w z \mathbf{v} \cdot \mathbf{n}_i) dS$$
$$-\int_{S_o} ((p + \Delta p) \mathbf{v} \cdot \mathbf{n}_o + \gamma_w (z + \Delta z) \mathbf{v} \cdot \mathbf{n}_o) dS$$
(3)

where, S_i and S_o are the inlet and outlet boundary surfaces of the control volume, having outer unit normal vector denoted by \mathbf{n}_i and \mathbf{n}_o ; p and $p + \Delta p$ are the static pressures at the inlet and outlet boundary surfaces; z and $z + \Delta z$ are the elevations at the inlet and outlet boundary surfaces; \mathbf{v} is the flow velocity; and γ_w is the unit weight of water. Five assumptions were made while developing Eq. (3) at the control volume scale: (i) the energy is mainly dissipated by viscous shear at the direct vicinity of the solid particles, (ii) the change in thermal energy at the control volume scale is negligible when compared to the mechanical energy expended by the flow in

eroding the particles, therefore the fluid temperature is considered constant,

(iii) the system is adiabatic, (iv) a steady-state flow is considered, and (v)

the flow is considered laminar. The validity of such assumptions have been

demonstrated in Marot et al. (2012), Sibille et al. (2015), Kodieh et al. (2021),

and Gelet and Marot (2022).

The instantaneous cumulative expended flow energy at time t can be calculated as the integral of the flow power over time:

$$E_{flow}(t) = \int_{t}^{t+\Delta t} P_{flow}(t)dt \tag{4}$$

One can define the flow power density and flow energy density as $\bar{P}_{flow}(t) = P_{flow}(t)/V$ and $\bar{E}_{flow}(t) = E_{flow}(t)/V$, respectively (V is the control volume).

Then, according to Eq. (4):

$$\bar{E}_{flow}(t) = \int_{t}^{t+\Delta t} \bar{P}_{flow}(t)dt. \tag{5}$$

Wang et al. (2024) proposed a constitutive relationship between the flow energy density $\bar{E}_{flow}(t)$ and the soil erosion rate per unit volume \dot{m} :

$$\dot{m} = \alpha \sinh \left(\beta \ \bar{E}_{flow} \right)$$
 (6)

with α and β given as:

$$\alpha = 2\rho_{dry} \frac{k_B T}{h_P} \exp\left(-\frac{\Delta F}{RT}\right)$$

$$\beta = \frac{\lambda}{Sk_B T}$$
(7)

where ρ_{dry} is the dry bulk density of the soil, k_B the Boltzmann's constant (1.38 × 10⁻²³ J/K), T the temperature in K, h_P the Planck's constant

 $(6.624 \times 10^{-34} \ J/s)$, ΔF the free activation energy, R the universal gas constant $(8.3144 \ J \cdot K^{-1} \cdot mol^{-1})$, λ the displacement of the flow unit per crossing of an energy barrier (with $2.8 \times 10^{-10} \ m$ as a reasonable assumed value which is the diameter of an oxygen ion according to Mitchell et al. (1969)), and S the number of flow units per unit area.

Remark: For a soil at a given temperature, the parameter α is a function of the dry bulk density ρ_{dry} and the activation energy ΔF of the soil, with the former being a function of the porosity and the latter demonstrated to be a soil property (Mitchell and Soga, 2005). The parameter β is a function of the number of bonds per unit area S, which has been demonstrated to be a function of the average effective stress in the soil (Mitchell et al., 1969). For a given soil, one can perform erosion tests while maintaining the same porosity, temperature, and confining stress to experimentally establish the values of α and β .

20 4. Model Implementation

1 4.1. Dual Random Lattice Model

This work exploits a three-dimensional DRLM framework for simulating temporal and spatial evolution of BEP in GFPI. Random lattice models are an attractive alternative to continuum approaches for modeling various civil engineering problems including transport problems (Bolander and Sukumar, 2005; Fascetti et al., 2016, 2018; Fascetti and Oskay, 2019a; Kozicki and Tejchman, 2008). The fundamental idea behind this class of numerical methods, which follows the pioneering work of Hrennikoff (1941), is that the three-dimensional behavior of a solid can be resolved on a dense lattice of

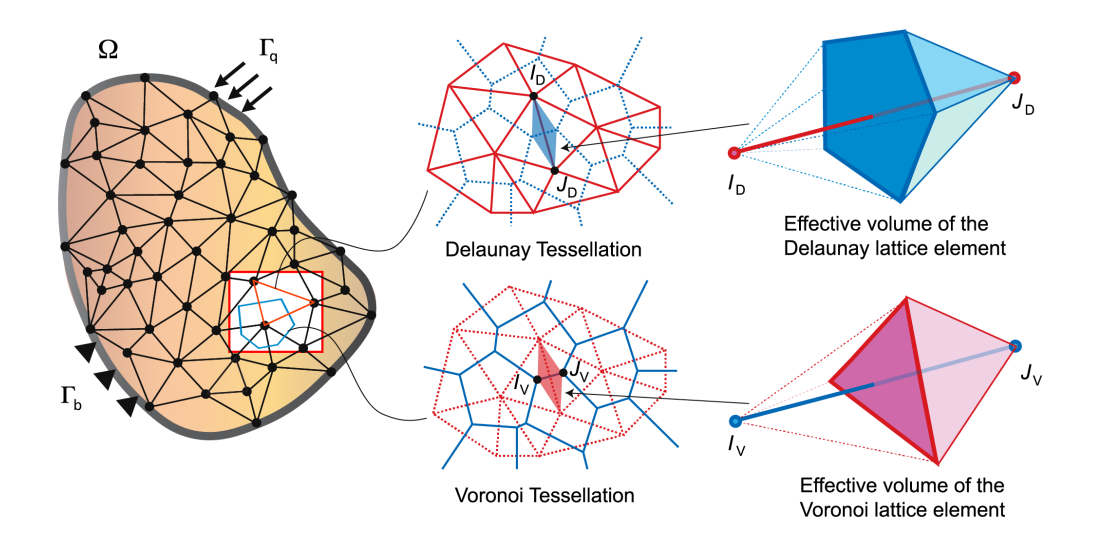


Figure 2: Graphical interpretation of the dual random lattice model

one-dimensional elements. In the context of simulating BEP, the main advantages of this approach include the following: (1) the solution of the governing equations is evaluated on a dense network of 1-dimensional lattice elements, which simplifies the derivation of the constitutive law; (2) the discrete nature of the model enables the representation of localized phenomena such as erosion; and (3) the spatial randomness of the lattice provides a substantial mesh independence (Kozicki and Tejchman, 2008). A thorough description of the main features of this modeling framework may be found in Fascetti and Oskay (2019a).

The DRLM exploits the geometrical features of the Delaunay and Voronoi tessellations of a 3D domain (see Fig. 2). Consider a randomly distributed set of nodes in a given 3D domain. The randomly distributed pointset can be obtained by randomly generating 3-D coordinates sampled from a uniform probability distribution function, as described in Fascetti and Oskay (2019a).

The Delaunay triangulation is a tessellation performed on the pointset such that none of the points lies inside the circumsphere of any tetrahedron in the triangulation. The Voronoi diagram, on the other hand, is the geometrical tessellation on the set of node points that associates each point with a polyhedron composed of all the points that are closer to that point than 248 any other in the pointset (Okabe et al., 1994). The two tessellations hold 249 the fundamental property of being dual, meaning that each edge in the De-250 launay tessellation is associated with a unique Voronoi area, and vice versa. 251 The areas on both lattices also hold the property of being orthogonal to the corresponding edge in the dual tessellation. This property is of fundamental 253 importance in computing the gradients of the field variable resolved on the 254 lattices, as described in the following. 255

Based on the aforementioned properties, a prevalent feature of the proposed DRLM approach is that the field variable h is simultaneously resolved on both the Delaunay and Voronoi lattice networks. This allows for 3-dimensional features of the solution (such as gradients) to be accurately evaluated, whereas traditional lattice approaches can only resolve this information at the 1-dimensional level of the lattice struts.

256

257

258

260

As derived in Fascetti and Oskay (2019a), the nonlinear diffusion problem defined by Eq. (1) can be written in compact form as:

$$\Psi \equiv \mathbf{M} \frac{d\mathbf{h}}{dt} + \mathbf{K}(h)\mathbf{h} - \mathbf{f} = 0$$
 (8)

where \mathbf{M} is the global mass matrix, \mathbf{h} the hydraulic head vector, $\mathbf{K}(h)$ the global diffusion matrix, and \mathbf{f} the force vector. The expressions for these relevant matrices were derived in the previous work by the authors (Fascetti

267 and Oskay, 2019a):

$$\mathbf{K}_{e} = \int_{\Omega} \mathbf{B}^{T} D \mathbf{B} d\Omega = \int_{l_{e}} D A_{e}(\mathbf{x}) \mathbf{B}^{T} \mathbf{B} dx = \frac{D A_{e}^{*}}{l_{e}} \begin{bmatrix} 1 & -1 \\ -1 & 1 \end{bmatrix}$$

$$\mathbf{M}_{e} = \int_{\Omega} \mathbf{N}^{T} \mathbf{N} d\Omega = \int_{l_{e}} A_{e}(\mathbf{x}) \mathbf{N}^{T} \mathbf{N} dx = \frac{V_{e}}{6} \begin{bmatrix} 2 & 1 \\ 1 & 2 \end{bmatrix}$$

$$\mathbf{f}_{e} = -\int_{\Omega_{q}} \mathbf{q} \mathbf{N}^{T} d\Omega_{q} = \begin{bmatrix} -q_{I} A_{e} \\ -q_{J} A_{e} \end{bmatrix}$$

$$(9)$$

where, V_e is the value of the effective volume of the current element, \mathbf{N} is the vector containing the element shape functions and \mathbf{B} the vector of their derivatives.

Remark: Although the element matrices in Eq. (9) take similar form as those reported in Grassl and Bolander (2016), Grassl et al. (2013), and Šavija et al. (2013), such works introduced a phenomenological correction parameter in the calculation of the matrix \mathbf{M} to ensure consistent calculation of the volume of the domain. In this work, the exact value of V_e is calculated by connecting the vertices of the resisting areas with the two ends of their associated elements (see Fig. 2), therefore conservation of volume is satisfied exactly.

Discretization in time is performed by means of the Crank-Nicolson method (Lewis et al., 2004):

$$\mathbf{M}\frac{\mathbf{h}^{n+1} - \mathbf{h}^n}{\Delta t} + \frac{1}{2} \left(\mathbf{K}^{n+1} \mathbf{h}^{n+1} + \mathbf{K}^n \mathbf{h}^n - \mathbf{f}^{n+1} - \mathbf{f}^n \right) = 0$$
 (10)

where Δt is the time step size and superscripts indicate the time step count (1 $\leq n \leq n_s t$, with $n_s t$ the total number of steps). The Crank-Nicholson

method is a semi-implicit scheme and unconditionally stable (Thomas, 2013).

Due to the presence of decaying spurious oscillation in the solution of the

transient problem, the maximum allowable time step size is set to:

$$\Delta t = \frac{l_{min}^2}{2D} \tag{11}$$

where l_{min} is the minimum value of the lattice element length in the mesh. It is worth noting that the temporal evolution of BEP is a dynamic process, therefore it is resolved as a transient problem in the numerical simulations. 288 This aspect of the numerical implementation is not in contrast with the 289 steady-state flow assumption when deriving the closed form solution for the flow power (see Eq. (3)) which has the physical meaning of assuming that the kinetic energy of the fluid does not change (i.e., it is negligible with respect to the change in energy induced by viscous effects). This assumption 293 is only required to derive a closed form solution for the power of flow, as 294 originally demonstrated in Marot et al. (2012), Sibille et al. (2015), Kodieh 295 et al. (2021), and Gelet and Marot (2022).

A key characteristic of the DRLM is simultaneous computation of transport behavior on both the Delaunay and Voronoi lattices for more accurate computation of hydraulic gradient. The local response gradients predicted by the lattice shape functions vanish along the direction orthogonal to the lattice element. By resolving the field variable (i.e., the hydraulic head h) on both assemblies, DRLM can approximate the gradient field at the orthogonal direction, therefore augmenting the local gradient calculation. Figure 3 illustrates a Voronoi lattice element $A_V - B_V$ and its dual triangular facet $A_D - B_D - C_D$ (the subscripts D and V indicate Delaunay and Voronoi ele-

297

299

300

302

303

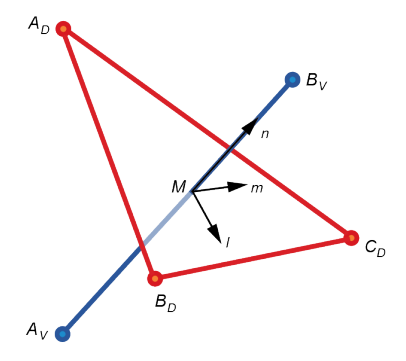


Figure 3: A Voronoi lattice element and its dual triangular facet formed by three Delaunay elements

ments, respectively). The component of the gradient in the direction parallel to the element (\mathbf{n} direction) is calculated on the Voronoi element (hence, \mathbf{i}_V), while the components on the plane orthogonal to the element (i.e., the plane of the resisting area) is obtained from the computed hydraulic head values at the Delaunay nodes (hence, \mathbf{i}_D).

The resultant gradient is obtained by:

311

$$\mathbf{i} = \mathbf{i}_V + \mathbf{i}_D = \mathbf{n} \frac{h_{B_V} - h_{A_V}}{l_e} + \frac{1}{2A_e} \mathbf{n} \times (h_{A_D} \mathbf{e}_{BC} + h_{B_D} \mathbf{e}_{CA} + h_{C_D} \mathbf{e}_{AB}) \quad (12)$$

where **n** is the unit vector along the Voronoi element; \mathbf{e}_{AB} , \mathbf{e}_{BC} , \mathbf{e}_{CA} are the unit vectors along the facet edges; h_{AV} , h_{BV} , h_{AD} , h_{BD} , h_{CD} are the hydraulic head values evaluated from solving the transport problem on both lattices. With the calculated resultant hydraulic gradient, the volumetric flow energy \bar{E}_{flow} in the effective volume can be calculated using Eqs. (3) and (4). It is important to include the Δz term in Eq. (3) while calculating the flow power, as a result of the fact that this term represents the change in elevation of

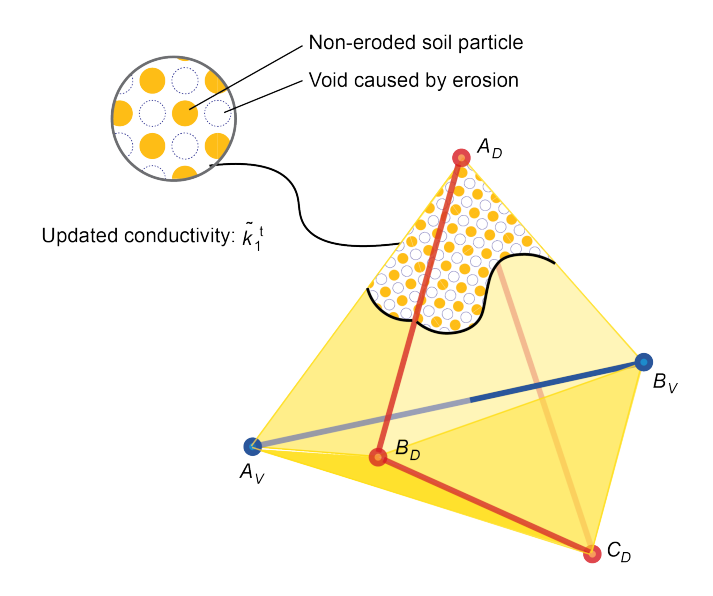


Figure 4: Erosion of a Voronoi lattice unit and update of its conductivity (updated soil matrix interpreted as collections of color-coded spheres)

the seepage flow through the effective volume ($\Delta z > 0$ for a downward flow direction and $\Delta z < 0$ otherwise), yielding significant effects on the predicted erosion rates.

2 4.2. Coupled Degradation in Dual Lattice Networks

As a result of the erosion process being described on the dual Delaunay and Voronoi lattices, it is of fundamental importance to accurately capture the changes in the material characteristics (i.e., the change in diffusivity due to the development of erosion) in both lattices throughout the simulations. As described in the previous section, the gradient of the hydraulic head field is resolved at the mid-point of each Voronoi lattice element (Point M in Fig. 3). The sub-assembly composed of a Voronoi element and the corresponding triangular Delaunay facets (see Fig. 4) constitutes the fundamental flow unit

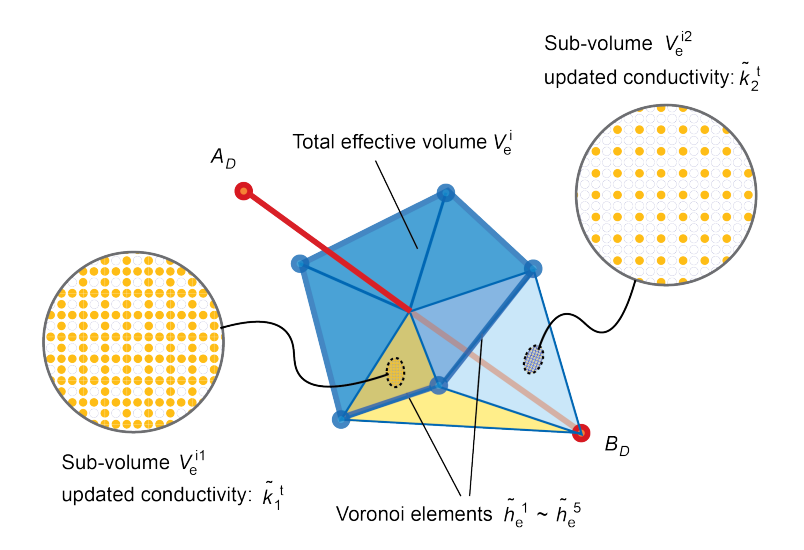


Figure 5: Volumetric averaging algorithm for computation of updated conductivity of a Delaunay unit from its dual Voronoi elements

resolved at the dual lattices level. The constitutive law is then exercised to evaluate the erosion rate at such material point (Eq. 6). Figure 4 depicts 332 an idealized representation of soil degradation under erosion conditions. The 333 yellow-colored dots represent non-eroded soil particles, while the dashed blue spheres represent voids created by the erosion process. The severity of soil 335 erosion is indicated by the number of eroded particles, represented by the 336 dashed blue spheres. As a result of the erosion process, updated values for 337 porosity and conductivity are computed. In order to correctly resolve the 338 non-linear process through the DRLM approach, this manuscript proposes an algorithm for the computation of coupled time-dependent degradation of the dual lattices.

From mass conservation, the following relationship between the rate of

342

change in porosity and the particle erosion rate holds:

$$\frac{\partial \phi(\mathbf{x}, t)}{\partial t} = \frac{\dot{m}}{\rho_s} \tag{13}$$

By combining Eqs. (6) and (13), the rate of change in porosity can be calculated from the following constitutive relationship:

$$\frac{\partial \phi(\mathbf{x}, t)}{\partial t} = \frac{1}{\rho_s} \alpha \sinh \left(\beta \ \bar{E}_{flow}(\mathbf{x}, t) \right)$$
 (14)

The rate of change in porosity of the effective volume of a Voronoi unit at any time t can be calculated via Eq. (14) and the associated hydraulic conductivity k of the effective volume is then evaluated from the updated soil porosity by means of the Kozeny-Carman equation. Figure 4 illustrates a conceptual representation of the updated soil structure of a Voronoi element $A_V - B_V$ and the effective volume it forms with its dual triangular Delaunay facet $A_D - B_D - C_D$ corresponding to an updated hydraulic conductivity k_1^t . The updated hydraulic conductivity field for the entire Voronoi lattice can be obtained by computing the updated hydraulic conductivity of every Voronoi lattice unit. A strategy for updating conductivity on the Delaunay lattice also needs to be devised. We propose that such value be computed as the weighted average of the Voronoi elements constituting the associated polygonal resisting area. This proposed algorithm is visually depicted in 358 Fig. 5. The weight of each Voronoi element \tilde{h}_e^j (e.g., j=1 to 5 in the case of 359 Fig. 5) is computed from the ratio of the volume of the tetrahedron associated 360 with the Voronoi element V_e^{ij} (formed by the four end nodes of $A_V B_V$ and the associated Delaunay element \tilde{h}_e^j) to the total effective volume V_e^i . This can be expressed mathematically as follows:

$$k_i^t = \frac{\sum_{j=1}^{n_i} \tilde{k}_j^t V_e^{ij}}{\sum_{j=1}^{n_i} V_e^{ij}} = \frac{\sum_{j=1}^{n_i} \tilde{k}_j^t V_e^{ij}}{V_e^i}$$
(15)

where k_i^t is the hydraulic conductivity of the effective volume Δ_e^i associated with Delaunay element h_e^i at time t, \tilde{k}_j^t the hydraulic conductivity of effective volume $\tilde{\Delta}_e^j$ associated with Voronoi element \tilde{h}_e^j at time t (\tilde{h}_e^j forms one of the edges of the polygonal resisting area of Δ_e^i), V_e^{ij} volume of the tetrahedron associated with \tilde{h}_e^j , V_e^i total volume of Δ_e^i , and n_i the total number of edges (Voronoi elements) in the polygonal resisting area of effective volume Δ_e^i . Note that in three dimension, the value of n_i varies across different Delaunay elements.

$_{372}$ 4.3. Modeling Procedure

385

The three-dimensional domain Ω is first constructed by means of a CAD 373 software. Then Delaunay tesellation of this domain is generated with a maximum tetrahedron volume criterion using the open-source TetGen library (Si, 375 2020). Next, the Voronoi diagram is constructed by connecting the centers of the circumshperes of every Delaunay tetrahedron. Finally, special treatments are needed on the discretization of the domain boundaries. As 378 introduced by Fascetti and Oskay (2019a), the circumcenters pertaining to 379 external tetrahedra (those lying on an external surface of the domain) are 380 mirrored with respect to the specific external surface. Only the part of the resulting Voronoi diagram inside the domain is kept as a new diagram while the rest part is removed. In this way, the Voronoi elements at the boundary are orthogonal to the surface.

After the dual lattice networks are constructed, each BEP simulation

requires the following steps:

405

406

407

408

409

410

- 1. A transient analysis is first performed until hydraulic equilibrium conditions are attained in the specimen for the given initial imposed heads $(h(\mathbf{x},0)=h_0(\mathbf{x}))$. In this analysis, the hydraulic conductivity of the soil is assumed to be constant and does not degrade to soil erosion $(k(\mathbf{x},0)=k_0)$ for all elements). Also, no degradation zone is assumed at this stage.
- 2. The hydraulic conductivity of all the lattice elements within a user-393 defined pipe initiation zone is amplified (i.e., $k(\mathbf{x},0) = m_p k_0$ for $\mathbf{x} \in$ 394 Ω_{ini} , where m_p is the user-defined amplification factor for conductivity 395 in the initiation zone and Ω_{ini} is the part of the domain defined as 396 the initiation zone accounting for a downstream exit condition). The 397 initiation zone with increased hydraulic conductivity creates a condi-398 tion of flow concentration, therefore increasing the hydraulic gradient 399 in the associated lattice elements. A second transient analysis is then 400 performed until hydraulic equilibrium is reattained in the domain after 401 initiation has been introduced. Soil degradation is still assumed not 402 taking place in this stage with hydraulic conductivity of all elements 403 remaining constant. 404
 - 3. Simulation of time evolution of BEP is performed by solving the nonlinear transport problem with the coupled degradation algorithm on the lattices embedded to account for time-dependent soil erosion. At each time step, soil degradation is evaluated in the following four sub-steps:

 (i) the hydraulic gradient field is computed by employing Eq. (12); (ii) the values of local flow energy density are evaluated through Eqs. (3)

and (4); (iii) the values of hydraulic conductivity of the Voronoi elements are updated based on changes in values of element porosity computed using Eq. (14) with the flow energy values calculated from sub-step (ii) and the Kozeny-Carman equation; (iv) the updated values of conductivity of the Delaunay elements are calculated from the updated conductivity field of the Voronoi lattice according to Eq. (15). The flow energy is recalculated at every time step with the updated conductivity field, and it is used to evaluate the degradation rate so as to update the conductivity values. A limit porosity criterion is adopted to account for the physical concept that only up to a certain fraction of the solid skeleton can be mobilized during the erosion process; such value represents the maximum local porosity attained for fully piped conditions (Fascetti and Oskay, 2019a). A Voronoi sub-assembly is therefore flagged as "piped" when its porosity reaches the maximum allowable value. The network formed by the piped elements indicates the erosion path. The simulation is considered complete when the pipe propagates to the upstream side or when hydraulic equilibrium is achieved in the domain (i.e., piping stops).

29 5. Comparison with Experimental Results

411

412

413

414

415

416

417

418

419

420

421

422

423

424

425

426

427

428

This section presents the assessment of performance of the proposed numerical method with simulations of experimental results reported in the literature. The experiments and specimens used for simulations are first described and values of modeling parameters are discussed. Then, sensitivity of the model to mesh density is analyzed before comparisons of the simulated

results and experimental observations are presented.

6 5.1. Calibration of Model Parameters

The set of experiments used to evaluate the capabilities of the model 437 comprises backward erosion piping tests on cylindrical sand specimens, as 438 reported in Robbins et al. (2018). A saturated sand specimen with length 439 958 mm was contained in an acrylic cylinder with internal diameter of 76.2 mm. The cylinder was closed with O-ring-sealed acrylic end plates bolted at the two ends to create a water-tight, unidirectional flow environment. The upstream end plate contains a porous filter to diffuse flow as it enters the sample and to prevent loss of soil close to the flow entrance tubing. The downstream side of the sample has a slope formed at the natural angle of repose of the soil, to ensure a shortest seepage path at the top of the cylinder and induce pipe initiation and propagation along the top surface of the sample. The upstream and downstream hydraulic heads were applied through two constant-head water tanks connected to the two ends of the sample. With a known pipe path along the top surface, local hydraulic pressures were continuously monitored by means of pressure ports installed at 100 mm intervals. 451 Temporal pipe progression was visually monitored via high-resolution video 452 recording aided by dye injection in the fluid. The sand under study had an 453 initial void ratio of 0.61, an initial relative density of 0.79, and the grain sizes were between standard U.S. sieves No.70 and No.40. The testing parameters which are reported in Robbins et al. (2018) were assigned directly 456 to the corresponding model parameters. The initial values of the other in-457 put parameters required in the simulations were adopted from the calibrated values reported in Wang et al. (2024) and were further refined by means of

Table 1: Model parameters

Parameter	Value
Length of specimen	958.0 mm
Diameter of specimen	$76.2 \ mm$
Global hydraulic gradient	0.4100
Initial porosity	0.3790
Initial conductivity	$6.2\times10^{-4}\ m/s$
Initial specific storage	$7.2 \times 10^{-5} \ m^{-1}$
Limit porosity c	0.7536
$lpha^c$	5.94×10^4
eta^c	1.00×10^{-3}

Note: ^ccalibrated with experimental results

a calibration procedure based on the pipe progression speed observed in the experiments. The calibrated parameters fell into the ranges of values as reported in the literature (Wang et al., 2024). All the material parameters are reported in Table 1.

4 5.2. Mesh Sensitivity Analysis

A sensitivity analysis has been carried out to quantify the effect of mesh density (i.e., the number of Delaunay points used to create the computational domain) on the obtained results. The goal of the analysis is to identify a lattice resolution with satisfactory accuracy while maintaining acceptable com-

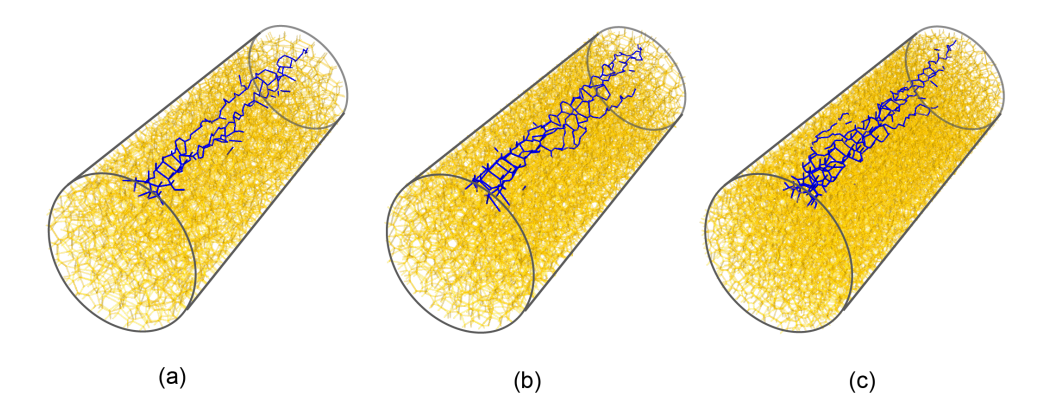


Figure 6: Visualizations of models with number of Delaunay nodes of: (a) 1,513, (b) 2,213, and (c) 3,177 (erosion path is indicated by piped elements colored in blue)

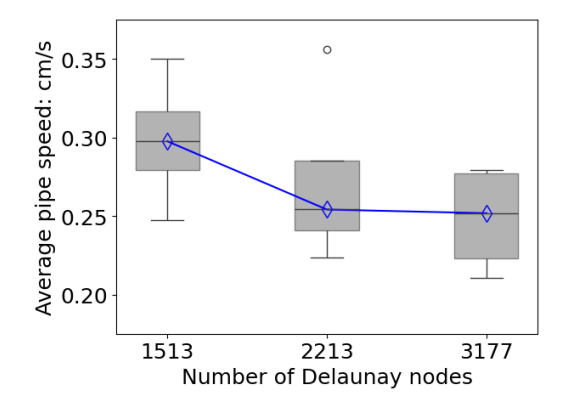


Figure 7: Study on lattice resolution

putational efficiency, in a way that is analogous to mesh convergence analyses commonly employed in the finite element method (Patil and Jeyakarthikeyan, 2018). The model parameters used in this analysis are the same as those listed in Table 1, except for the length of the specimen, which was set to 200.0 mm in order to save computational resources. Simulations with different lattice resolutions were performed and the results with number of Delaunay nodes nd = 1,513, 2,213, 3,177 are shown in Fig. 6 and Fig. 7.

Figure 6 provides visualizations of the three models with the computed 476 erosion paths highlighted (indicated by piped elements in blue). Figure 7 reports the values of average piping speed in the three models. Such speeds 478 are calculated as $L_i/\Delta t$, where L_i is the length of a specified portion of the 479 domain, and Δt is the time it takes the pipe to traverse such length. For each 480 model, such values are computed on four consecutive 40.0 mm-long segments along the longitudinal direction of the specimen. The results reported in Fig 7 482 were used to examine mesh sensitivity in the proposed approach. The length 483 of the domain used in the sensitivity analysis is 200.0 mm; the first 30.0 mm 484 and the last 10.0 mm of the specimen were excluded from the calculations 485 of pipe speed, due to the fact that the measurements would be relatively less accurate as a result of imposed boundary conditions. As can be seen in Fig. 7, the median of the average pipe progression speed converges at the Delaunay 488 node number of 2,213 (corresponding to $V_{max}^{tet} = 150 \text{ } mm^3$). Therefore, a lattice resolution with a maximum tetrahedron volume V_{max}^{tet} of 150 mm^3 is adopted for the simulation reported below.

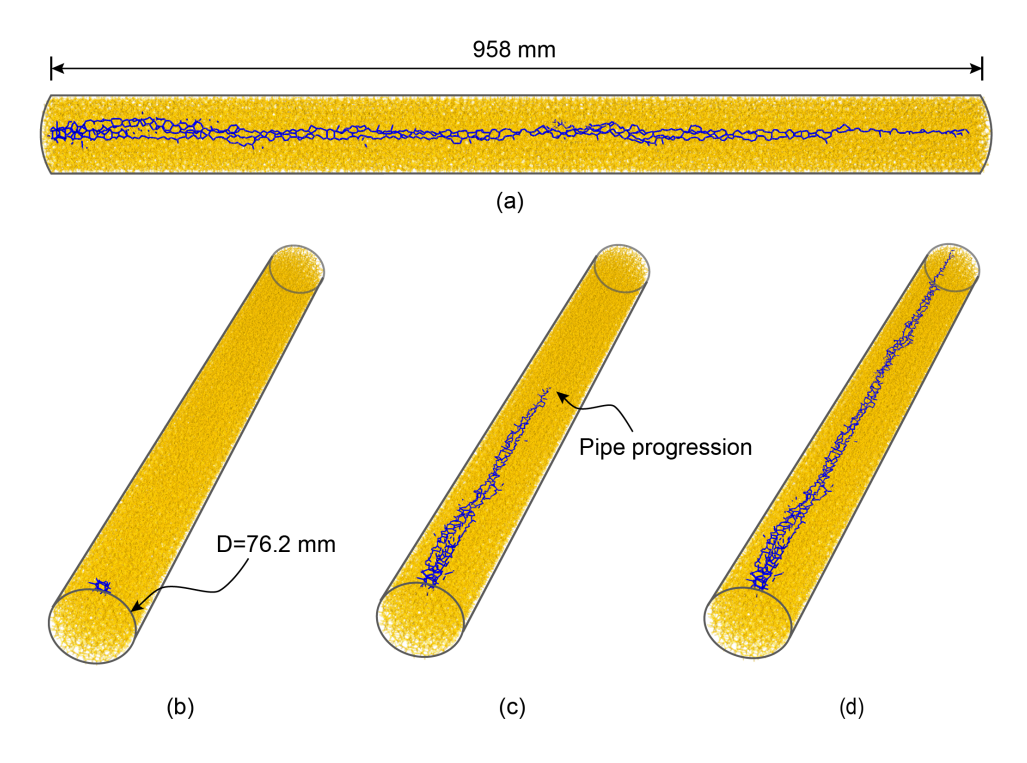


Figure 8: Topology of erosion path over time: (a) a top view at t=480~sec, and three oblique views at (b) t=0~sec, (c) t=250~sec, and (d) t=480~sec

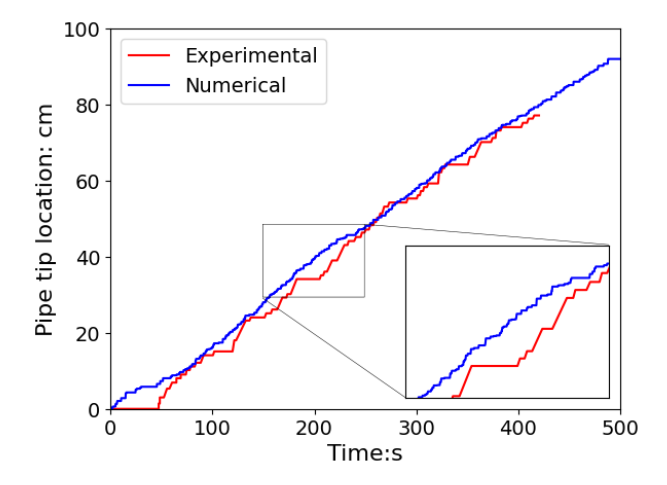


Figure 9: Experimental and numerical pipe tip location over time (experimental data available in Robbins et al. (2018))

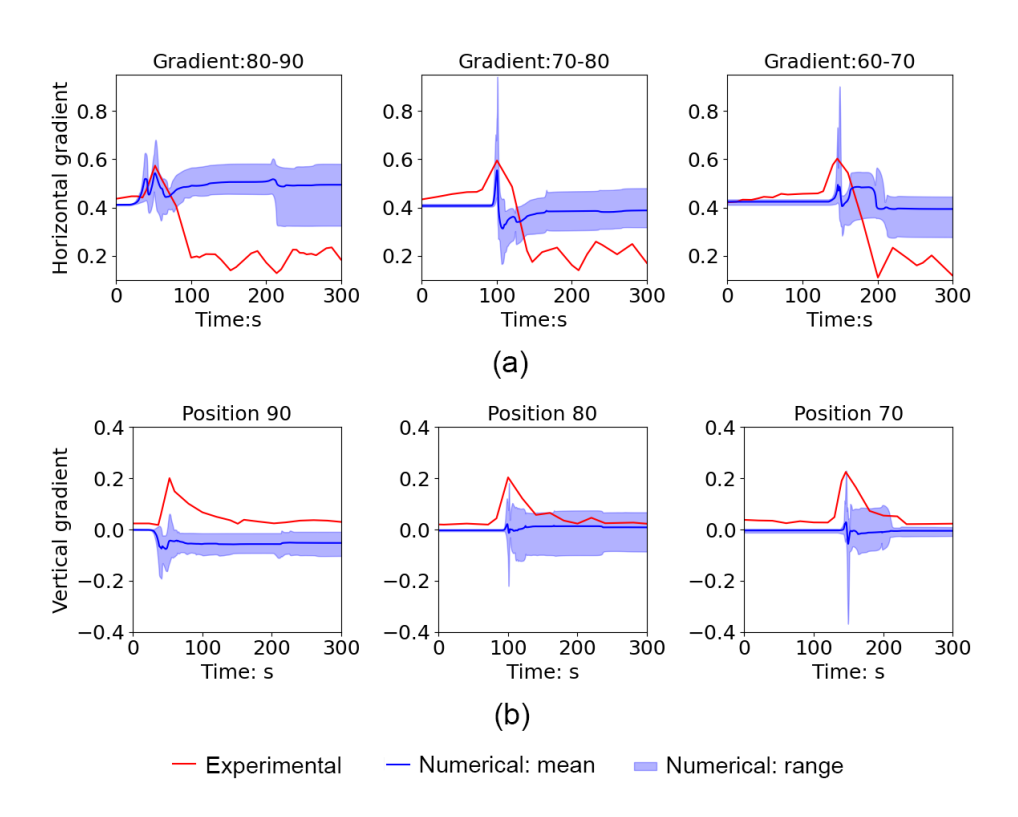


Figure 10: Experimental and numerical evolution of local hydraulic gradient (mm/mm) in the domain: (a) horizontal hydraulic gradient, and (b) vertical hydraulic gradient (experimental data obtained from Robbins et al. (2018))

5.3. Numerical Results

Numerical simulation results are presented and their comparisons with the 493 experimental findings are discussed in this subsection. Figure 8 illustrates the progressive development of the erosion path predicted by the model over 495 time. A quantitative description of pipe advancement over time is shown 496 in Fig. 9, where experimental observations from Robbins et al. (2018) are 497 included for comparison. As shown in Fig. 8, the proposed numerical model 498 is capable of capturing the spatial advancement of piping erosion. In Fig. 8, the erosion path is predicted as a single horizontal network formed by inter-500 connected Voronoi elements of which the hydraulic conductivity has reached 501 the maximum value (i.e., the "piped elements"). Along the longitudinal 502 direction, most of the cross sections of the pipe path comprise up to four branches of parallel Voronoi elements. This branching feature of the pipe path can be attributed to the tessellated representation of the simulation domain. 506

As shown in Fig. 9, the time evolution of the pipe tip location predicted with the proposed DRLM model matches the experimental results well. Consistency is evident not only in the similar pipe progression speed but also in the step-wise patterns in both curves, with the experimental observations showing more prominent steps. The proposed approach describes the time-dependent erosion of soil particles as a rate process, resulting in a trend that shares this fundamental feature with the experimental evidence. Moreover, discretization on dense 1-dimensional lattice networks allows for substantial mesh-independence and representation of the 3-dimensional characteristics of BEP, with the erosion paths not being constrained on element bound-

ary and/or pre-defined paths, as in most available numerical models. The variation in step sizes between the two curves can be attributed to the differing methods used for identifying the pipe tip, with the simulation relying on porosity analysis while the experiment used visual observations based on camera recording. The agreement between the numerical and experimental pipe tip advancement demonstrates the model's capability in capturing temporal pipe progression during BEP and supports the hypothesis that soil erosion can be described as a rate process.

Figure 10 reports comparisons between the experimental and numerically 525 evaluated hydraulic gradients in the specimen. Evolution of the local gradi-526 ents illustrate very similar patterns in the simulation as those observed in the 527 experiment. It is important to note that the gradient values are calculated 528 differently in the numerical simulations than in the experiments (Robbins et al., 2018). The local gradients are computed in the simulation on the individual Voronoi elements by means of the algorithm introduced in Section 4, while 531 the experiments estimated local gradients based on hydraulic pressure measurements from adjacent pressure ports and their relative distances (Robbins 533 et al., 2018). The reason that the numerical gradients were not computed in the same way as in the experimental study is because to accurately simulate the hydraulic pressure measurements with pressure transducers connected to openings on the acrylic cylinder, complex boundary conditions at these locations need to be considered which is out of the scope of this study. Therefore, the local gradients as computed in the lattice elements were used for comparisons with the experimental results. The corresponding gradient values from the simulation as illustrated in the Fig. 10 are extracted from Voronoi

lattices located in three box-shaped measuring regions corresponding to the locations of the pressure transducers installed on the laboratory specimen. As shown in Fig. 10(a), the evolution of local horizontal gradients at the three locations from both the experiment and simulation show significant increases as the pipe tip approaches. The different resolutions in computing the local gradients as discussed above could explain the slight difference between the 547 peak magnitudes of the experimental and numerical gradients, as shown in Fig. 10. Moreover, in the simulation curves of horizontal gradients labeled as 80-90 and 60-70 as shown in Fig. 10(a), there are more than one peak while the experimental data from each measuring location contain only one peak. 551 This is likely due to local branching in the simulation pipe path with different 552 branches reaching the measurement areas at different time steps. One other 553 discrepancy is that in the experiment, the local horizontal gradients dropped to around 0.2 in the later stage of the test, while they asymptotically tended 555 to the initial applied gradient in the simulation. This is because in the exper-556 iment, the upstream hydraulic head was no longer maintained constant after the pipe reached the upstream side, as reported in Robbins et al. (2018). Similar conclusions can be drawn from the comparison of the local vertical gradients, as shown in Fig. 10(b). The good agreements between the experimental and numerical vertical gradients, as shown in Fig. 10(b), demonstrate 561 the capability of the proposed model in accurately capturing local gradients in three dimensions.

6. Conclusions

586

A novel three-dimensional dual random lattice modeling approach for the simulation of BEP in GFPI has been proposed herein. The groundwater seepage is evaluated by solving the nonlinear diffusion problem on two inde-567 pendent dual lattice networks. The first main novelty of this study is that a constitutive relationship between the flow energy density and particle erosion rate is adopted in the simulations, alleviating known issues with available numerical methods. The relationship is based on the theory of rate processes, 571 and describes BEP as successive particle rearrangements caused by the en-572 ergy expended by the seepage flow. This formulation based on fundamen-573 tal granular physics is distinct from previous empirical approaches, which primarily relied on experimental observations and provided semi-empirical descriptions of BEP. The adopted constitutive relationship was incorporated into the DRLM to enable computations of rates of local soil degradation so as to calculate time evolution of BEP in the computational domain. The 578 proposed volume-based averaging algorithm to calculate coupled degradation of the dual lattices is of critical importance to maintain consistency in the calculations, when employing dual lattice calculations. Furthermore, the proposed methodology, while applied to simulation of BEP, is fundamentally applicable to a wide array of problems involving computation of the gradi-583 ents of a field variable, and therefore potentially impacts a broader range of problems. 585

The capabilities of the proposed numerical model were investigated by comparison with experimental observations available in the literature. A mesh resolution study was performed to identify the optimal mesh density to be employed in the simulations. Good agreement was observed between
the numerical and experimental data in all the quantitative metrics reported
in the experiments, namely: (1) spatial advancement of piping erosion, (2)
temporal evolution of the pipe tip, and (3) dynamic evolution of local hydraulic gradients. The proposed model has been demonstrated to be capable
of accurately capturing the aforementioned aspects of time evolution of BEP
in saturated sand embankments in 3-D. In a previous study, Fascetti and
Oskay (2019b) developed a machine learning-based reduced order modeling
(ROM) framework to perform regional-scale risk assessment of geotechnical
flood protection systems by means of training the ROM with data obtained
from local-scale simulations. A similar approach can be leveraged to incorporate the local-scale model proposed herein in a multiscale framework capable
of predicting time evolution of BEP at the global scale.

602 CRediT authorship contribution statement

Zhijie Wang: Methodology, Investigation, Formal analysis, Visualization, Validation, Writing – original draft. Caglar Oskay: Conceptualization, Methodology, Validation, Writing – review & editing. Alessandro
Fascetti: Conceptualization, Methodology, Resources, Investigation, Validation, Supervision, Writing – review & editing.

Declaration of competing interest

The authors declare that they have no known competing financial interests or personal relationships that could have appeared to influence the work reported in this paper.

Data availability

Data will be made available on request.

References

- Allan, R., 2018. Backward erosion piping. PhD Thesis, The University of
 New South Wales, Sydney, Australia.
- Bligh, W.G., 1910. Dams, barrages and weirs on porous foundations. Eng.
 News. 64(26), 708-710.
- Bolander, J.E., Sukumar, N., 2005. Irregular lattice model Rev. В. 71, 094106. quasistatic crack propagation. Phys. 620 https://doi.org/10.1103/physrevb.71.094106. 621
- Bonelli, S., Benahmed, N., 2010. Piping flow erosion in water retaining structures: inferring erosion rates from hole erosion tests and quantifying the failure time. IECS 2010, 8th ICOLD European Club Symposium Dam Safety-Sustainability in a Changing Environment, Sep 2010, Innsbruck, Austria. 6 p. hal-00555648.
- Cheng, N. S., 2004. Analysis bedload of transport in flows. laminar Adv. Water Resour. 27(9),937-942. 628 https://doi.org/10.1016/j.advwatres.2004.05.010. 629
- El Shamy, U., Aydin, F., 2008. Multiscale modeling of flood-induced piping in river levees. J. Geotech. Geoenviron. Eng. 134(9), 1385-1398. https://doi.org/10.1061/(asce)1090-0241(2008)134:9(1385).

- Eyring, H., 1936. Viscosity, plasticity, and diffusion as exam-
- ples of absolute reaction rates. J. Chem. Phys. 4(4), 283-291.
- https://doi.org/10.1063/1.1749836.
- ⁶³⁶ Fascetti, A, Bolander, J.E., Nisticò, N, 2018. Lattice discrete particle model-
- ing of concrete under compressive loading: multiscale experimental ap-
- proach for parameter determination. J. Eng. Mech. 144(8), 04018058.
- https://doi.org/10.1061/(asce)em.1943-7889.0001480.
- 640 Fascetti, A, Feo, L, Nisticò, N, Penna, R, 2016. Web-flange behav-
- ior of pultruded GFRP I-beams: a lattice model for the inter-
- pretation of experimental results. Compos. B. Eng. 100, 257–69.
- 643 https://doi.org/10.1016/j.compositesb.2016.06.058.
- 644 Fascetti, A., Oskay, C., 2019. Dual random lattice modeling
- of backward erosion piping. Comput. Geotech. 105, 265-276.
- https://doi.org/10.1016/j.compgeo.2018.08.018.
- Fascetti, A., Oskay, C., 2019. Multiscale modeling of backward erosion piping
- in flood protection system infrastructure. Comput-Aided Civ. Inf. 34(12),
- 649 1071-1086. https://doi.org/10.1111/mice.12489.
- 650 Federal Emergency Management Agency (FEMA), 2019. Fact
- Sheet: Myths and Facts About Flood Insurance (June 11, 2019).
- https://www.fema.gov/press-release/20230425/fact-sheet-myths-and-
- facts-about-flood-insurance.
- Fleshman, M.S., Rice, J.D., 2013. Constant gradient piping test apparatus

- for evaluation of critical hydraulic conditions for the initiation of piping.
- Geotech. Test. J. 36(6), 834-846. https://doi.org/10.1520/gtj20130066.
- Foster, M., Fell, R., Spannagle, M., 2000. The statistics of embank-
- ment dam failures and accidents. Can. Geotech. J. 37(5), 1000-1024.
- https://doi.org/10.1139/t00-030.
- 660 Fujisawa, K., Murakami, A., Nishimura, S.I., 2010. Numerical analy-
- sis of the erosion and the transport of fine particles within soils
- leading to the piping phenomenon. Soils Found. 50(4), 471-482.
- https://doi.org/10.3208/sandf.50.471.
- 664 Gelet, R., Marot, D., 2022. Internal erosion by suffusion on cohesionless gap-
- graded soils: Model and sensibility analysis. Geomech. Energy Environ.
- 31(100313). https://doi.org/10.1016/j.gete.2022.100313.
- 667 Glasstone, S., Laidler, K.J., Eyring, H., 1941. The theory of rate process:
- The kinetics of chemical reactions, viscosity, diffusion and electrochemical
- phenomena. New York and London: McGraw-Hill Book Company, Inc.
- 670 Grassl, P., Bolander, J.E., 2016. Three-dimensional network model for cou-
- pling of fracture and mass transport in quasi-brittle geomaterials. Materi-
- als. 9(9), 782. https://doi.org/10.3390/ma9090782.
- 673 Grassl, P., Fahy, C., Gallipoli, D., Bolander, J., 2013. A lattice model for liq-
- uid transport in cracked unsaturated heterogeneous porous materials. VIII
- International Conference on Fracture Mechanics of Concrete and Concrete
- 676 Structures, Toledo, Spain. https://doi.org/10.1201/b14393-75.

- 677 Green, D.H., Wang, H.F., 1990. Specific storage as a poroelastic coefficient.
- Water Resour. Res. 26(7), 1631–1637. doi:10.1029/WR026i007p01631.
- 679 Gularte, R.C., Kelly, W., Nacci, V., 1980. Erosion of cohesive sediments as
- a rate process. Ocean Eng. 7(4), 539-551. https://doi.org/10.1016/0029-
- 8018(80)90051-7.
- Hagerty, D., Curini, A., 2004. Impoundment failure seepage analyses. Envi-
- ron. Eng. Geosci. 10(1), 57-68. https://doi.org/10.2113/10.1.57.
- Hanses, U., 1985. Zur Mechanik der Entwicklung von Erosionskanälen in
- geschichtetem Untergrund unter Stauanlagen: The mechanics of the devel-
- opment of erosion pipes in a layered substratum beneath dams. Grundbau-
- Inst., d. Techn. Univ.
- 688 Hrennikoff, A, 1941. Solution of problems of elasticity by the framework
- method. J. Appl. Mech. 12, 169–75.
- 690 Indraratna, B., Muttuvel, T., Khabbaz, H., 2009. Modelling the erosion rate
- of chemically stabilized soil incorporating tensile force-deformation charac-
- teristics. Can. Geotech. J. 46(1), 57-68. https://doi.org/10.1139/T08-103.
- 693 Khilar, K.C., Fogler, H.S., Gray, D.H., 1985. Model for piping-
- plugging in earthen structures. J. Geotech. Eng. 111(7), 833-846.
- 695 https://doi.org/10.1061/(ASCE)0733-9410(1985)111:7(833).
- 696 Kodieh, A., Gelet, R., Marot, D., Fino, A., 2021. A study of suffusion kinetics
- inspired from experimental data: comparison of three different approaches.
- 698 Acta Geotech. 16, 347-365. https://doi.org/10.1007/s11440-020-01016-5.

- 699 Kozicki, J., Tejchman, J., 2008. Modelling of fracture process in con-
- crete using a novel lattice model. Granul. Matter. 10, 377-388.
- 701 https://doi.org/10.1007/s10035-008-0104-4.
- Lewis, R.W., Nithiarasu, P., Seetharamu, K.N., 2004. Fundamentals of the finite element method for heat and fluid flow. John Wiley & Sons.
- 704 Marot, D., Le, V.D., Garnier, J., Thorel, L., Audrain, P., 2012
- Study of scale effect in an internal erosion mechanism: centrifuge
- model and energy analysis. Eur. J. Environ. Civ. Eng. 16(1), 1-19.
- 707 https://doi.org/10.1080/19648189.2012.667203.
- Michalowski, R., Wang, Z., Nadukuru, S., 2018. Maturing of con-
- tacts and ageing of silica sand. Géotechnique. 68(2), 133-145.
- https://doi.org/10.1680/jgeot.16.p.321.
- Mitchell, J.K., 1964. Shearing resistance of soils as a rate process.
- J. Soil Mech. Found. Div., Am. Soc. Civ. Eng. 90(1), 29-61.
- https://doi.org/10.1016/0022-4898(64)90023-0.
- Mitchell, J.K., Campanella, R.G., Singh, A., 1968. Soil creep as a rate
- process. J. Soil Mech. Found. Div., Am. Soc. Civ. Eng. 94(1), 231-253.
- https://doi.org/10.1061/jsfeaq.0001085.
- Mitchell, J.K., Singh, A., Campanella, R.G., 1969. Bonding, effective stresses,
- and strength of soils. J. Soil Mech. Found. Div., Am. Soc. Civ. Eng. 95(5),
- 1219-1246. https://doi.org/10.1016/0022-4898(70)90065-0.
- Mitchell, J.K., Soga, K., 2005. Fundamentals of soil behavior. Hoboken, NJ,
- USA: John Wiley & Sons.

- Negrinelli, G., 2015. Investigation of the process of seepage and backward erosion piping under dikes in heterogeneous sands. PhD Thesis, University of Brescia, Brescia, Italy.
- Negrinelli, G., Van Beek, V., Ranzi, R., 2016. Experimental and numerical investigation of backward erosion piping in heterogeneous sands. Scour and Erosion: Proceedings of the 8th International Conference on Scour and Erosion (Oxford, UK, 12-15 September 2016).
- C., Ojha, Singh, V., Adrian, D., 2003. Determination of crithead in soil piping. J. Hydraul. Eng. 129(7),511-518. 730 https://doi.org/10.1061/(asce)0733-9429(2003)129:7(511). 731
- Okabe, A., Boots, B., Sugihara, K., 1994. Nearest neighbourhood operations with generalized Voronoi diagrams: a review. Int. J. Geogr. Inf. Syst. 8(1), 43-71. https://doi.org/10.1080/02693799408901986.
- Patil, H., Jeyakarthikeyan, P.V., 2018. Mesh convergence study and estimation of discretization error of hub in clutch disc with integration of ANSYS.
 In IOP Conf. Ser. Mater. Sci. Eng. 402, 012065.
- Peng, S., Rice, J.D., 2020. Measuring critical gradients for soil loosening and initiation of backward erosion-piping mechanism. J. Geotech. Geoenviron. Eng. 146(8), 04020069. https://doi.org/10.1061/(ASCE)GT.1943-5606.0002277.
- Pol, J. C., Kanning, W., Jonkman, S. N., 2021. Temporal development of backward erosion piping in a large-scale experiment. J. Geotech. Geoen-

- viron. Eng. 147(2), 04020168. https://doi.org/10.1061/(asce)gt.1943-5606.0002415.
- Rahimi, M., Shafieezadeh, A., Wood, D., Kubatko, E. J., 2021.
- A physics-based approach for predicting time-dependent progression
- length of backward erosion piping. Can. Geotech. J. 58(7), 995-1004.
- 749 https://doi.org/10.1139/cgj-2019-0854.
- Reddi, L.N., Bonala, M., Lee, I., 2000. Comparison of internal and surface
- erosion using flow pump tests on a sand-kaolinite mixture. Geotech. Test.
- J. 23(1), 116-122. https://doi.org/10.1520/gtj11129j.
- Richards, K.S., Reddy, K.R., 2012. Experimental investigation of initia-
- tion of backward erosion piping in soils. Géotechnique. 62(10), 933-942.
- https://doi.org/10.1680/geot.11.p.058.
- Richards, K.S., Reddy, K.R., 2007. Critical appraisal of piping phe-
- nomena in earth dams. Bull. Eng. Geol. Environ. 66, 381-402.
- https://doi.org/10.1007/s10064-007-0095-0.
- Robbins, B., Griffiths, D., 2021. A two-dimensional, adaptive finite element
- approach for simulation of backward erosion piping. Comput. Geotech.
- 129, 103820. https://doi.org/10.1016/j.compgeo.2020.103820.
- Robbins, B.A., 2016. Numerical modeling of backward erosion piping. Ap-
- plied numerical modeling in geomechanics. 2016, 551-558.
- 764 Robbins, B.A., van Beek, V.M., López-Soto, J.F., Montalvo-
- Bartolomei, A.M., Murphy, J., 2018. A novel laboratory test for

- backward erosion piping. Int. J. Phys. Model. Geotech. 18(5), 266-279.
- 767 https://doi.org/10.1680/jphmg.17.00016.
- Rotunno, A.F., Callari, C., Froiio, F., 2019. A finite element method for
- localized erosion in porous media with applications to backward pip-
- ing in levees. Int. J. Numer. Anal. Methods Geomech. 43(1), 293-316.
- 771 https://doi.org/10.1002/nag.2864.
- ⁷⁷² Šavija, B., Pacheco, J., Schlangen, E., 2013. Lattice modeling of chloride
- diffusion in sound and cracked concrete. Cem. Concr. Compos. 42, 30–40.
- https://doi.org/10.1016/j.cemconcomp.2013.05.003.
- Schmertmann, J.H., 2000. The no-filter factor of safety against pip-
- ing through sands. In Judgment and innovation: the heritage
- and future of the geotechnical engineering profession. (Silva, F.
- ⁷⁷⁸ & Kavazanjian Jr., E. (eds.)), pp. 65-132. Reston, VA: ASCE.
- https://doi.org/10.1061/9780784405376.006.
- 780 Sellmeijer, J.B., 1988. On the mechanism of piping under impervious struc-
- tures. PhD Thesis, Delft University of Technology, Delft, Netherlands.
- 782 Si, H., 2020. TetGen, a Quality Tetrahedral Mesh Generator and 3D De-
- launay Triangulator (Version 1.6 User's Manual). Weierstrass Institute for
- Applied Analysis and Stochastic, Berlin, Germany.
- 785 Sibille, L., Lominé, F., Poullain, P., Sail, Y. & Marot, D., 2015. In-
- ternal erosion in granular media: direct numerical simulations
- and energy interpretation. Hydrol. Processes. 29(9), 2149-2163.
- 788 https://doi.org/10.1002/hyp.10351.

- Thomas, J.W., 2013. Numerical partial differential equations: finite difference methods. New York, USA: Springer.
- van Beek, V., Robbins, B., Rosenbrand, E., van Esch, J., 2022. 3D modelling
- of backward erosion piping experiments. Geomech. Energy Environ. 31,
- 793 100375. https://doi.org/10.1016/j.gete.2022.100375.
- van Beek, V., Van Essen, H., Vandenboer, K., Bezuijen, A., 2015. Devel-
- opments in modelling of backward erosion piping. Géotechnique. 65(9),
- 740-754. https://doi.org/10.1680/geot.14.p.119.
- van Beek, V.M., 2015. Backward erosion piping: Initiation and progression.
- PhD Thesis, Delft University of Technology, Delft, Netherlands.
- van Beek, V.M., De Bruijn, H., Knoeff, J., Bezuijen, A., Förster, U., 2010.
- Levee failure due to piping: A full-scale experiment. In Proceedings 5th
- International Conference on Scour and Erosion (ICSE-5), (Burns, S.E.,
- Bhatia, S.K., Avila, C.M.C. & Hunt, B.E. (eds.)). San Francisco, USA:
- ASCE. https://doi.org/10.1061/41147(392)27.
- van Esch, J., Sellmeijer, J., Stolle, D., 2013. Modeling transient groundwater
- flow and piping under dikes and dams. 3rd international symposium on
- computational geomechanics (ComGeo III). 9.
- Vandenboer, K., van Beek, V., Bezuijen, A., 2014. 3D finite element method
- 808 (FEM) simulation of groundwater flow during backward erosion piping.
- Front. Struct. Civ. Eng. 8, 160-166. https://doi.org/10.1007/s11709-014-
- 810 0257-7.

- Vandenboer, K., Celette, F., Bezuijen, A., 2019. The effect of sudden critical
- and supercritical hydraulic loads on backward erosion piping: small-scale
- experiments. Acta Geotech. 14, 783-794. https://doi.org/10.1007/s11440-
- 018-0756-0.
- Wang, D., Fu, X., Jie, Y., Dong, W., Hu, D., 2014. Simulation of pipe pro-
- gression in a levee foundation with coupled seepage and pipe flow domains.
- Soils Found. 54(5), 974-984. https://doi.org/10.1016/j.sandf.2014.09.003.
- Wang, Z., Oskay, C., Fascetti, A., 2024. Backward Erosion Piping in
- Geotechnical Infrastructure: A Rate Process Perspective. Géotechnique.
- https://doi.org/10.1680/jgeot-2023-259. [In Press]
- White, C., 1940. The equilibrium of grains on the bed of a stream. Proc.
- Math. Phys. Eng. Sci. 174(958), 322-338.
- ⁸²³ Zeghal, M., El Shamy, U. 2004. A continuum-discrete hydromechanical anal-
- ysis of granular deposit liquefaction. Int. J. Numer. Anal. Meth. Geomech.
- 28(14), 1361–1383. https://doi.org/10.1002/nag.390.